

Intense structures of different momentum fluxes in turbulent channels

Kosuke Osawa*

Department of Engineering, Tokyo Institute of Technology, 2-12-1 Ookayama, Meguro-ku, Tokyo, Japan

Javier Jiménez

School of Aeronautics, Universidad Politécnica de Madrid, 28040 Madrid, Spain

(Dated: March 22, 2022)

The effect of different definitions of the momentum flux on the properties of the coherent structures of the logarithmic region of wall-bounded turbulence is investigated by comparing the structures of intense tangential Reynolds stress with those of the alternative flux proposed in [J. Jiménez, *J. Fluid Mech.* **809**, 585 (2016)]. Despite the fairly different statistical properties of the two flux definitions, it is found that their intense structures show many similarities, such as the dominance of ‘wall-attached’ objects, and geometric self-similarity. The new structures are wider, but not taller, than the classical ones, and include both high- and low-momentum regions within the same object. It is concluded that they represent the same phenomenon as the classical groups of a sweep, an ejection, and a roller, suggesting that these groups should be considered the fundamental coherent structures of the momentum flux. The present results show that the properties of these composite momentum structures are robust with respect to the definition of the fluxes.

I. INTRODUCTION

Understanding the physical mechanism of momentum transfer in wall turbulence is crucial both theoretically and in applications, because it is connected with the mechanical equilibrium of the flow and with the possible control of the wall friction. Traditionally, since the average of the tangential Reynolds stress over wall-parallel planes is equal to the total wall-normal transfer of streamwise momentum, its local value has been interpreted as a local momentum flux, and regions of intense Reynolds stress have been identified and studied as coherent structures of the momentum transfer. They are usually referred to as ‘quadrant’ structures [1–3], because they are associated with different quadrants in the joint probability density function (PDF) of two velocity components, and their spatial and temporal characteristics have come to be considered properties of the momentum transfer itself [1, 4].

However, it has been repeatedly pointed out that it is the divergence of the Reynolds stresses, and not the stresses themselves that enter the equations of motion [5, 6], and that the definition of local flux is ambiguous because any divergence-free flux field can be added to it without changing the physics. Recently, Jiménez [7] revisited this question, and studied in some detail a definition of the momentum flux which is ‘optimal’ in the sense of having a minimum integrated norm for a given divergence. Somewhat disturbingly, he found that the instantaneous fields and many of the statistical properties of the new fluxes differ considerably from those of the Reynolds stress, raising some doubts about whether the previously mentioned studies of coherent structures and, indeed, a lot of the effort dedicated to modeling locally the Reynolds stress tensor, may only apply to a particular flux definition, and be therefore largely irrelevant.

There is little in this new definition to make it better, or worse, than the classical Reynolds stress, although minimizing the norm should also help in minimizing any spurious flux component. Its real interest is that the new fluxes are different from the classical ones, although equally valid, so that any interpretation of properties that are not shared by the two definitions may be considered as physically ‘suspect’.

An obvious alternative would be to abandon the use of fluxes and stresses, and to fall back on their divergence. This approach was discussed in some detail in [7], and had been considered before [5, 6], although mostly from the point of view of modeling [8, 9]. It changes the character of the analysis, because fluxes are large-scale quantities, while their divergence is associated with smaller scales. The question is similar to whether to focus on the pressure or on the pressure gradient [10]. The gradient appears in the equations of motion and determines the acceleration of the fluid, but, as shown by Bernoulli’s equation, the pressure is more directly related to the velocities.

In the context of wall-bounded turbulence, the point-wise identification of the momentum flux with the Reynolds stress is the central assumption that allows us to scale the velocity fluctuations with the friction velocity, as well as to classify motions into active or inactive [11]. It is also behind classical quadrant analysis, including the idea that the properties of quadrants reflect those of the momentum flux, and therefore of the energy production. Thus, it

* osawa.k.ad@m.titech.ac.jp

TABLE I. Parameters of the channel flow databases. $L_x, L_z, 2h$ are the streamwise, spanwise and wall-normal domain size, respectively. $\Delta x, \Delta z$ are spatial resolutions, in terms of Fourier modes, and N_y is the number of wall-normal grid points. N_s is the number of snapshots used in the analyses.

Re_τ	L_x/h	L_z/h	Δx^+	Δz^+	N_y	N_s	Symbol	Ref.
934	8π	3π	11	5.7	385	20	none	[12]
2003	8π	3π	12	6.1	633	9	o	[13]

is important to determine whether it is at least approximately correct. To assess its ‘robustness’, we repeat here the identification and classification of intense structures using the new ‘optimal’ definition of momentum flux, and compare them with the coherent structures based on the classical Reynolds stress.

The organization of this paper is as follows. The simulations used for the analysis, and the identification criteria for the structures, are introduced in §II. The geometry of the identified structures is discussed in §III, and their relative position with respect to high- and low-momentum regions and to other flux structures is presented in §IV and §V. Finally §VI examines the conditional velocity fields relative to the new structures, and §VII concludes.

II. NUMERICAL EXPERIMENTS AND STRUCTURE IDENTIFICATION

We use data from direct numerical simulations of turbulent channel flow at two Reynolds numbers, periodic in the two wall-parallel directions and of half-height h . The streamwise, wall-normal and spanwise directions are x, y, z , respectively, and u, v, w are the corresponding components of the velocity fluctuations with respect to its mean. Overlines, $\overline{(\)}$, denote y -dependent ensemble averages, usually implemented as spatial averages over x, z planes and time. Whenever subindices are added to an average, they represent the variables over which the average is taken. Thus $\overline{(\)}_{xz}$ defines a time-dependent average over wall-parallel planes. The ensemble-averaged mean streamwise velocity is $U(y)$, and primes are reserved for the root-mean-square fluctuation intensities. Variables with a ‘+’ superscript are normalized in wall units, defined from the kinematic viscosity, ν , and from the friction velocity, u_τ , which is in turn defined from the shear stress at the wall as $u_\tau^2 = \nu \partial_y U|_{y=0}$. The friction Reynolds number is $Re_\tau = u_\tau h / \nu$.

The simulations use Fourier spectral discretization in (x, z) , dealiased by the 2/3 rule. The wall-normal discretization is Chebychev spectral for the lower-Reynolds-number case [12], and compact finite differences for the higher one [13]. Time stepping is third-order semi-implicit Runge–Kutta, keeping the mass flux constant. Some numerical parameters are collected in table I, and further details can be found in the original publications.

A. The momentum flux

We focus on the structures of the classical tangential Reynolds stress, uv , and of the corresponding optimal flux, ϕ_{xy} . Details of the computation of the ϕ_{ij} tensor can be found in [7], and will not be repeated here. Basically, it is a symmetric tensor that shares its divergence with the Reynolds stress,

$$\partial_j \phi_{ij} = \partial_j (u_i u_j), \quad (1)$$

while minimizing the norm

$$\int \phi_{ij} \phi_{ij} d^3 \mathbf{x}, \quad (2)$$

where the integral extends over the whole channel, indices range from x to z , and repeated indices imply summation. In general, because ϕ_{ij} has the same divergence as the classical Reynolds stress, it generates the same integrated flux across any closed surface. In particular, ϕ_{xy} plays the same role as uv , transferring streamwise fluctuating momentum along y , and the instantaneous integral of the two quantities over wall-parallel planes is identical, $(\phi_{xy})_{xz} = (uv)_{xz}$. This integral is the net result of fluxes that change sign locally, with some cancellation between positive and negative contributions. That only the divergence of the flux tensor enters the equations of motion suggests that at least some of this cancellation is arbitrary and could be avoided. The minimization of (2) is intended to avoid as much unnecessary cancellation as possible, and it was indeed found in [7] that there is much less momentum backscatter in the optimum ϕ_{xy} than in the classical Reynolds stress, and that a large part of the local intermittency of the Reynolds stress is not present in the optimal flux.

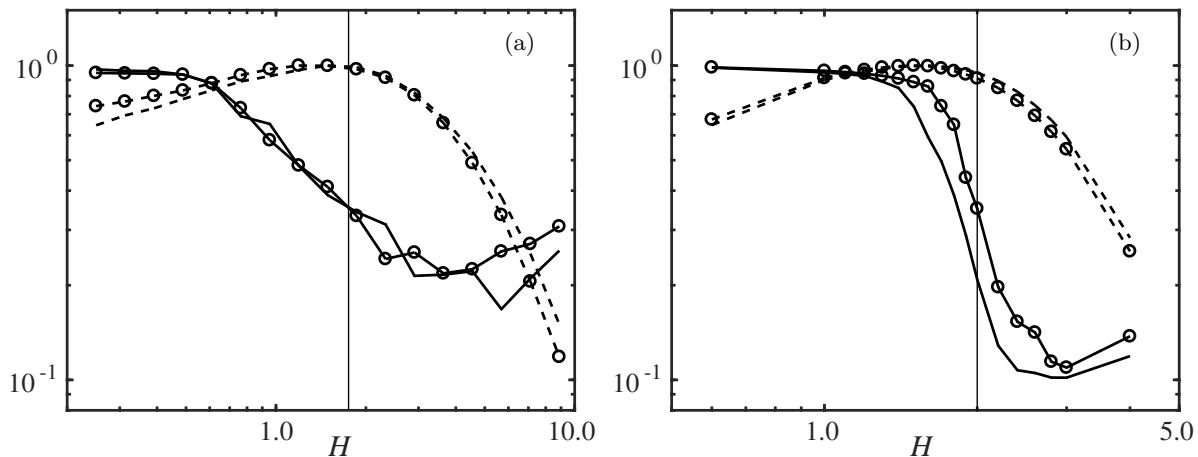


FIG. 1. Percolation diagram for the identification of: (a) Qs of uv , adapted from [2], and (b) Ops of ϕ_{xy} . The solid lines are the ratio of the volume of the largest object to the volume of all identified objects; the dashed ones are the ratio of the number of identified objects to the maximum number of objects. The vertical line is the nominal threshold: $H = 1.75$ in (a), and $H = 2$ in (b). Symbols denote the two Reynolds numbers, as in table I.

TABLE II. Number fraction of identified objects with respect to their total number, and volume fraction with respect to the flow domain. Superscripts show the sign of the mean momentum flux within each structure.

Re_τ	N_{Qs}^-	N_{Qs}^+	V_{Qs}^-	V_{Qs}^+	N_{Ops}^-	N_{Ops}^+	V_{Ops}^-	V_{Ops}^+
934	0.60	0.40	0.081	0.011	0.64	0.36	0.073	0.006
2003	0.61	0.39	0.073	0.020	0.67	0.33	0.068	0.008

B. The identification of structures

Intense structures of ϕ_{xy} are identified by the same method used in [2] for the quadrant structures of uv . Namely, the intense regions of a generic quantity q are extracted by thresholding,

$$|q| > Hf(y), \quad (3)$$

with respect to some y -dependent flow statistics $f(y)$. Each set of mutually contiguous points satisfying (3) is defined as an individual structure. The constant H is chosen using the percolation analysis developed in [14]. The threshold used for uv is the same as in [2],

$$|uv| > 1.75 u'(y)v'(y). \quad (4)$$

After some experimentation, the threshold for ϕ_{xy} was chosen to be

$$|\phi_{xy}| > 2.00 \phi'_{xy}(y). \quad (5)$$

Figure 1(a,b) shows that both thresholds are in the midst of the respective percolation transition. It was checked that the results presented below are qualitatively independent of the threshold as long as it is within the transition range ($1.4 < H < 2.4$ for ϕ_{xy}). It was also checked that using a different thresholding quantity, $f(y) = (\overline{\phi_{xy}^2})^{1/2} = (\phi_{xy}^{\prime 2} + \overline{\phi_{xy}^2})^{1/2}$, had a small effect on the properties of the structures. Recall that, although quantities such as u denote zero-mean fluctuations, neither ϕ_{xy} nor uv have zero mean. In what follows, the coherent structures identified for uv and ϕ_{xy} are denoted as Qs and Ops , respectively.

III. THE GEOMETRY OF INDIVIDUAL STRUCTURES

Table II shows the number and volume fraction occupied by the objects identified by the procedure explained above, oriented in each half of the channel with respect to their closest wall. With this notation, the average momentum

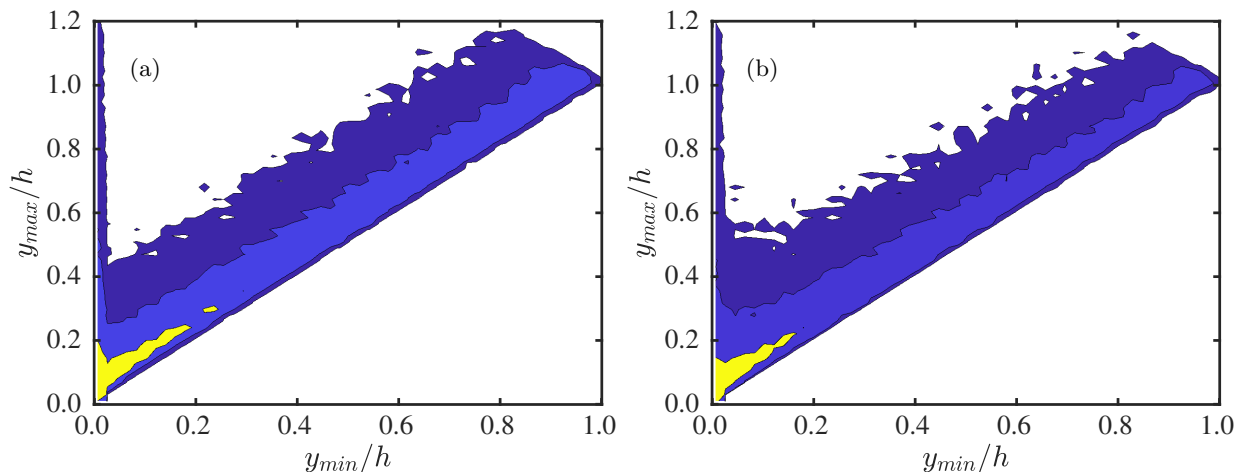


FIG. 2. Joint PDF of the distance from the closest wall to the bottom (y_{min}) and top (y_{max}) of the structures. (a) Q_s , (b) Ops . Contours include 40%, 90% and 98.8% of data. $Re_\tau = 934$.

flux is negative, and objects carrying a net negative momentum flux will be called co-gradient. Individual objects can carry either a net positive or a net negative flux, but table II shows that co-gradient ones are more common, both for wv and for ϕ_{xy} . They also tend to be larger than counter-gradient ones, as seen by the larger relative difference between the volume contributions of the two kinds, compared to their number frequency. In the case of Q_s , for which the sign of the velocity fluctuations is fixed by their definition, co-gradient objects are classified as ‘sweeps’ or ‘ejections’ [1] depending on whether their streamwise velocity fluctuation is positive or negative, respectively. In the case of Ops , that distinction is not clear, and the relation of Ops with the two types of Q_s will be one of the questions to be discussed below.

Each object is circumscribed within a parallelepipedic box aligned to the Cartesian axes, which is used to define both its position, and its dimensions Δ_x , Δ_z and $\Delta_y = y_{max} - y_{min}$, where y_{min} and y_{max} are the minimum and maximum distance of the object from the nearest wall, respectively. Figure 2 shows the joint probability density function (PDF) of y_{min} and y_{max} . Lozano-Durán et al. [2] showed that Q_s can be classified into two families based on their minimum distance from the wall. The ‘attached’ Q_s in the left-most side of the figure 2(a) have $y_{min}^+ < 20$, but some of them are very large, growing to be as tall as the channel half-height. The ‘detached’ structures in the diagonal band of figure 2(a) never approach the wall, and their height Δ_y depends little on the wall distance. The same classification into attached and detached families applies to vorticity [15] and velocity structures [16], with minor variations in the limiting y_{min} that separates the two families. In the logarithmic layer of channels, around 60% of the Reynolds stress is carried by attached Q_s , while detached objects carry a much smaller fraction of the total stress. In fact, it was shown in [2, 17] that detached objects are random fluctuations which are too small to couple with the mean shear, and that they are present in all shear flows. They are isotropically oriented, and do not collectively contribute to the mean momentum flux. Attached objects are also common features of shear flows, and they can even be identified in flows without walls [17]. They are large enough to couple with the mean shear, and are responsible for most of the mean momentum flux. This coupling also means that large co-gradient Q_s extract energy from the mean flow, which allows them to grow even larger. In essence, ‘attached’ objects are defined by being large, rather than by being attached to the wall, but the geometry of flows over walls is such that objects cannot grow to be large enough to couple with the shear without also hitting the wall [18].

As can be seen in figure 2(b), Ops also separate into attached and detached families. In the logarithmic layer, attached Ops carry 30% of the mean momentum flux, which is close to the overall contribution of all the Ops . Co-gradient detached Ops carry approximately 7% of the flux, which is partially compensated by about -2% from the counter-gradient ones. As in the case of Q_s , attached Ops are dominant, and we mostly focus on co-gradient attached objects in the following.

Especially relevant are attached objects that are large enough to reach above the buffer layer, $\Delta_y^+ > 100$, and are therefore largely inviscid. Most of the discussion in the previous paragraphs applies to these ‘tall’ objects. They were also the main focus of the discussion in [2, 15–17].

It should be mentioned at this point that the smaller contribution of the Ops to the total flux, when compared to the Q_s , is mainly, but not wholly, due to the choice of the identification threshold H . The total contribution of Q_s to the momentum flux varies from 95% to 30% as the threshold changes across the percolation range from $H = 1$ to $H = 3$, while that of the Ops only varies from 65% to 20% as H changes from 1.4 to 2.4. Overall, ϕ_{xy} is less

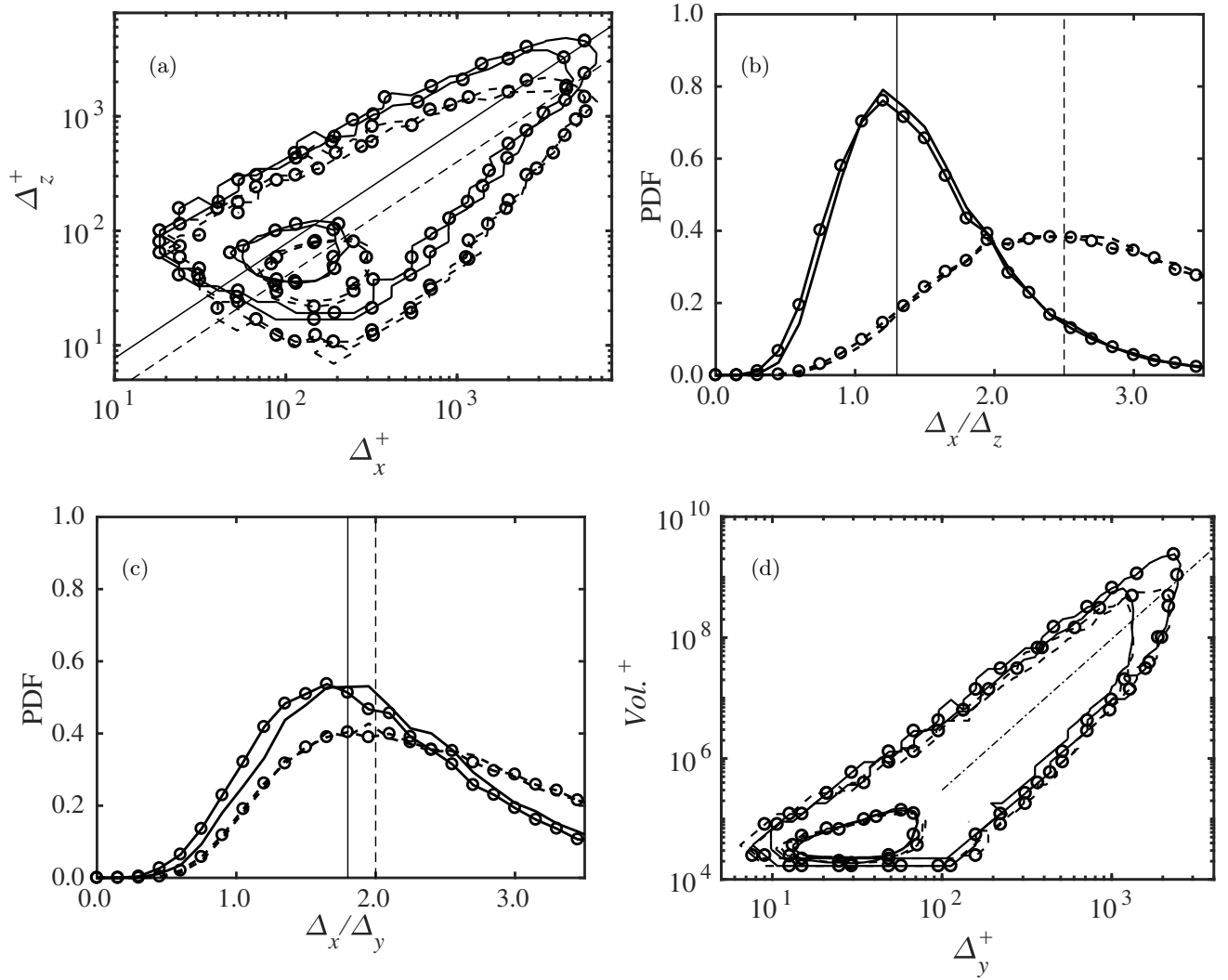


FIG. 3. (a) Joint PDF of the wall-parallel dimensions (Δ_x, Δ_z) of attached structures. Contours include 50% and 99.8% of the data. The two diagonals are $\Delta_x = 1.3\Delta_z$ and $\Delta_x = 2.5\Delta_z$. (b) PDF of the wall-parallel aspect ratio Δ_x/Δ_z of tall attached objects ($y_{min}^+ > 100$). The two vertical lines mark the peak value of the PDF, obtained by parabolic fitting: $\Delta_x/\Delta_z = 1.3$ and $\Delta_x/\Delta_z = 2.5$. (c) As in (b) for the wall-normal aspect ratio Δ_x/Δ_y of tall attached objects. The vertical lines are $\Delta_x/\Delta_y = 1.8$ and $\Delta_x/\Delta_y = 2.0$. (d) Joint PDF of the volume and height of attached structures. Contours include 50% and 99.8% of data. The diagonal line is $Vol. \propto \Delta_y^{2.5}$. In all figures, solid and dashed lines correspond to Ops and Qs , respectively, and symbols denote the two Reynolds numbers, as in table I.

intermittent than uv , and a given fraction of the momentum flux requires a larger volume in the former than in the latter [7].

The dimensions of attached Qs and Ops are compared in figure 3(a), which shows the joint PDF of the logarithms of the wall-parallel sizes of the attached objects, as determined from their bounding box. The PDF follows a linear trend in both cases, but with a different slope for Qs and for Ops . The PDFs of the aspect ratio Δ_x/Δ_z , shown in figure 3(b) for tall attached objects, indicate that the Ops are almost twice wider than the Qs . A similar linear relation applies to the wall-parallel and wall-normal dimensions of the objects, confirming that both Qs and Ops form self-similar families in the logarithmic layer, but figure 3(c) shows that the wall-normal aspect ratio of Qs and Ops is very similar. Ops are wider than Qs but not taller.

Figure 3(d) shows the joint PDF of the volume and height of attached Qs and Ops . For the tall objects defined above, the relation between Δ_y and the volume approximately follows a power law, similar in both structures. The exponent changes slightly with the Reynolds number, and with the range of wall-distances considered, but it is always close to 2.5, with a slight tendency to higher exponents in Ops than in Qs . If interpreted as a fractal dimension, it implies fairly full shell- or flake-like objects [2].

In all these results, it is important to note the excellent collapse of the two Reynolds numbers used in the study.

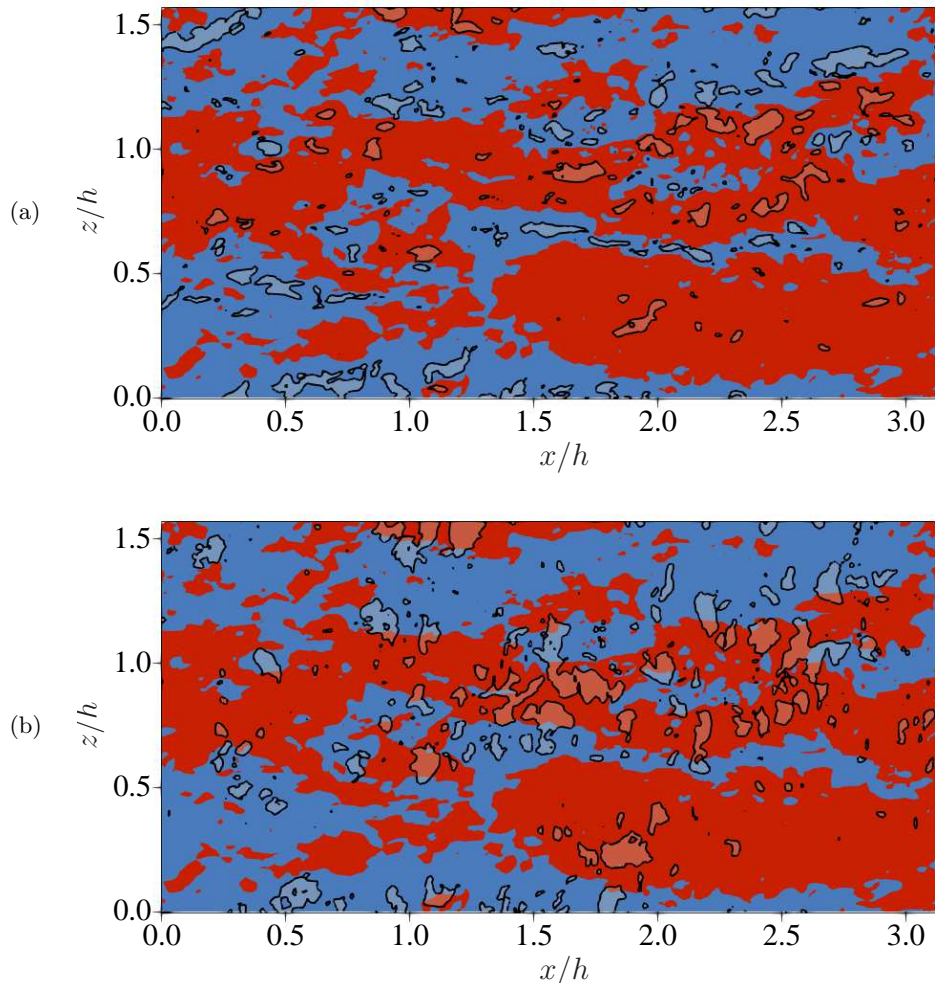


FIG. 4. (a) Snapshot of low/high-momentum regions (blue for $u < 0$, and red for $u > 0$), and wv above the identification threshold for Qs (translucent contour). Flow is from left to right. (b) As in (a), for Ops . $Re_\tau = 2003$ at $y/h = 0.10$.

IV. RELATION TO LOW- AND HIGH-MOMENTUM REGIONS

In the rest of the paper, we will only consider tall attached objects ($\Delta_y^+ > 100$) that do not extend beyond the logarithmic layer ($\Delta_y/h < 0.2$). This is the same restriction applied to Qs in [2], and will facilitate the comparison.

The first point to consider is the relation of Qs and Ops to the high- and low-momentum regions (streaks) of the flow. In the case of Qs , it follows from their definition that sweeps ($u > 0$) reside in high-speed regions, and ejections ($u < 0$) in low-speed ones. It was found in [2] that sweeps and ejections tend to be paired side by side, with each pair straddling the border between a high- and a low-speed streak. Figure 4(a) is a snapshot of u at $y^+ = 200$, showing how Qs are restricted to one or the other sign of u . The same snapshot is repeated in figure 4(b), but showing the contours of ϕ_{xy} , instead of wv . In contrast to Qs , the figure shows that many Ops intersect both a high- and a low-momentum region. This can be quantified by the volume fraction occupied by low-momentum points within each object,

$$F = \frac{\int_{\Omega_{u < 0}} dV}{\int_{\Omega_{u \geq 0}} dV + \int_{\Omega_{u < 0}} dV}, \quad (6)$$

where Ω is the interior of the object and subscripts represent conditioning by the sign of u . Objects with $F = 0$ are completely within a high-momentum region, and those with $F = 1$ are within a low-momentum one.

For the reasons mentioned above, most Qs are in one of these two limits, so that the PDF of F for Qs is essentially formed by two delta functions at $F = 0$ and $F = 1$. On the other hand, the PDF in figure 5(a) shows that the distribution for the Ops is more uniform. Except for an excess of purely low-momentum Ops , their PDF is

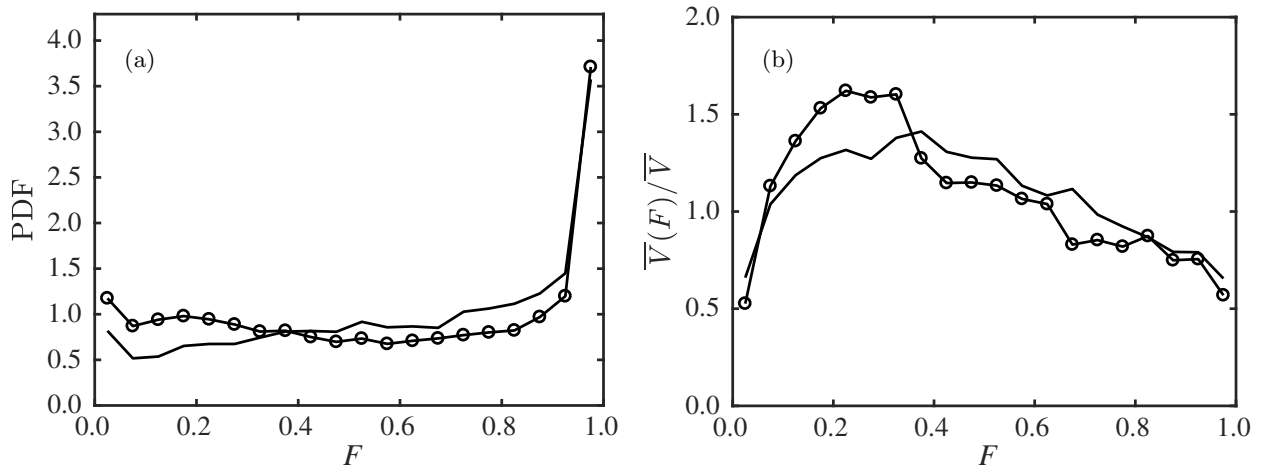


FIG. 5. (a) PDF of the low-momentum fraction, F , as defined in (6), for tall attached *Ops* in the logarithmic layer. (b) Conditionally averaged volume of *Ops* as a function of F , where the overline denotes averaging over all the tall attached objects in the logarithmic layer. Symbols denote the two Reynolds numbers, as in table I.

approximately uniform. Moreover, Figure 5(b) shows that ‘pure’ *Ops* tend to be smaller than those with mixed momentum regions, so that their contribution to the overall object volume is less than implied by their PDF. In fact, the number fraction of the pure *Ops* ($F < 5\%$ or $F > 95\%$) is 26% of the total, but their contribution to the volume is only 14%. Moreover, when all the tall attached objects are considered, including those taller than $\Delta_y/h = 0.2$, the volume fraction of the pure *Ops* is only 3%. The result is that, as opposed to *Qs*, the *Ops* cannot be classified into sweeps and ejections.

The reason for the excess of low-momentum *Ops* is unclear, but it is known that low-momentum regions in wall-bounded flows contain more coherent vortices than high-momentum ones [19], and that ejections, which are objects of low streamwise velocity, are more common than sweeps above the buffer layer [2]. There are several possible explanations for this inhomogeneity, ranging from artifacts due to using a uniform threshold across a non-uniform flow plane, to actual physics. The most likely reason, which is supported by informal visual inspection of individual flow fields, is that low-velocity regions are associated with positive wall-normal velocities, which bring active turbulence from the high-shear region near the wall, while high-velocity ones receive relatively quiescent flow from the low-shear region in the center of the channel.

V. THE RELATIVE POSITION OF OBJECTS

The relationships among different objects is discussed next by means of the PDF of their relative position, which is defined for object j relative to object i as the vector

$$\delta^{(ij)} = \frac{\mathbf{x}_c^{(j)} - \mathbf{x}_c^{(i)}}{\overline{\Delta}_y^{(ij)}}, \quad (7)$$

with components $\delta_k^{(ij)}$, $k = x \dots z$. Positions are referred to the center, $\mathbf{x}_c^{(i)}$, of the circumscribing box of object i , and lengths are normalized with the mean wall-normal height of the two objects, $\overline{\Delta}_y^{(ij)} = (\Delta_y^{(i)} + \Delta_y^{(j)})/2$. As in [2], only objects with similar size,

$$1/2 < \Delta_y^{(j)}/\Delta_y^{(i)} < 2, \quad (8)$$

are considered to be related, but we follow in this work the practice in [17] of compiling the PDFs using only the closest object to the reference one, instead of using all the neighbors satisfying (8), as was done in [2]. The statistical spanwise symmetry of the flow is used to improve the convergence of the PDFs.

Figure 6(a) shows the two-dimensional PDF of the relative position of the closest *Op* relative to another *Op*. Related *Ops* tend to be located streamwise from one another, separated by the mean streamwise length of the reference *Op*, and 85% of the *Ops* find another *Op* satisfying condition (8) at $Re_\tau = 2003$.

This arrangement is similar to the relative position of *Qs* of the same kind (e.g. sweep-sweep), but *Qs* of different kinds, such as a sweep and its closest ejection tend to form pairs aligned spanwise from one another. In the logarithmic

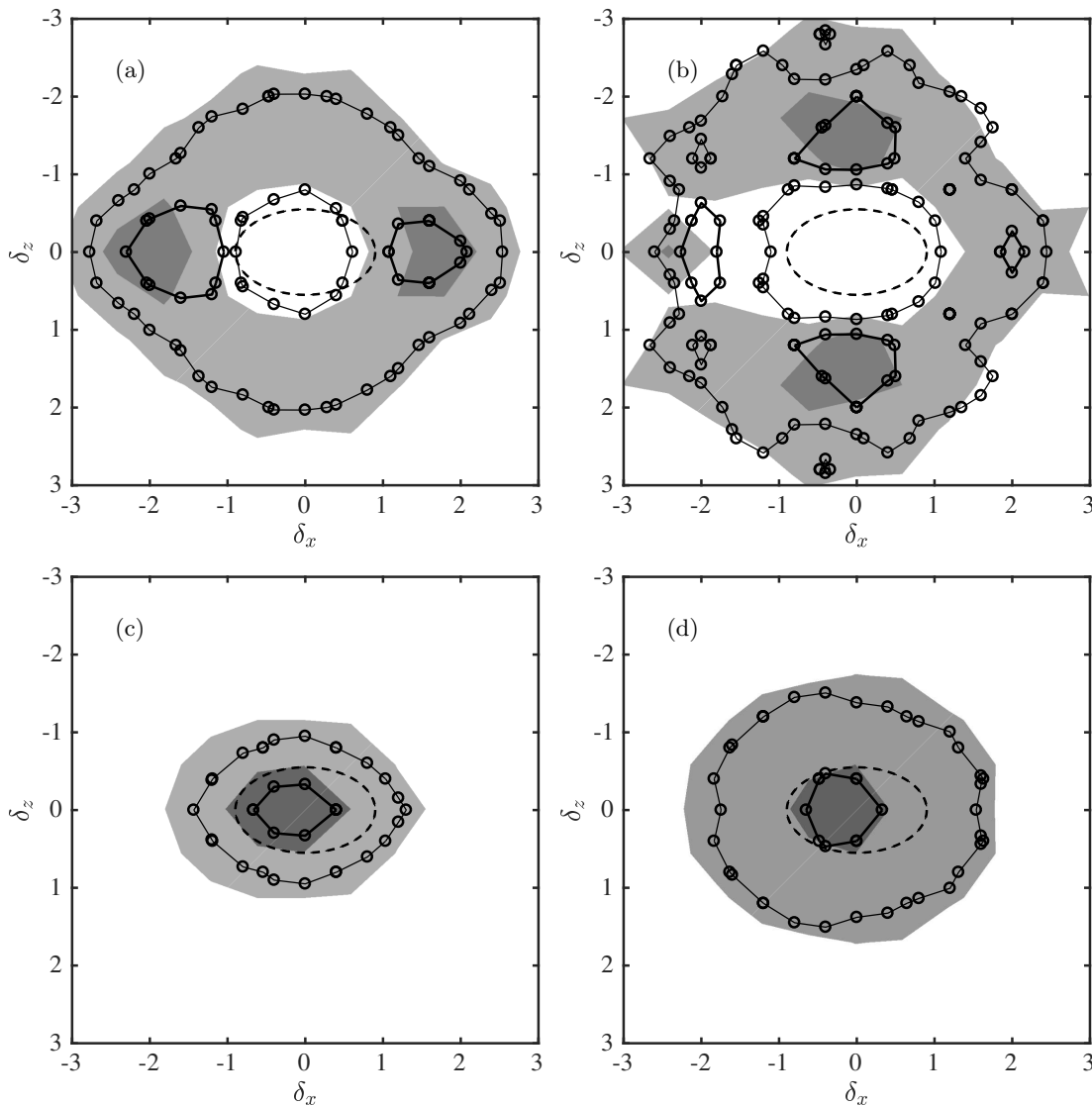


FIG. 6. Two-dimensional PDF of the relative position of: (a) Closest Op relative to another Op . (b) Closest low-momentum Op ($F \geq 0.5$) relative to a high-momentum Op ($F < 0.5$). (c) Closest Q relative to an Op . (d) Closest sweep-ejection Q -pair relative to an Op . Bold line contours and darker filled areas contain 10% of the data. Thinner contours and lighter areas contain 50% of the data. Shaded contours are $Re_\tau = 934$ and lines are $Re_\tau = 2003$. The dashed ellipses correspond to the mean size of the reference object.

layer, 80% of the Qs form such pairs, or similar composite structures [2]. We have seen that Ops cannot be classified into sweeps and ejections, but the relative position of predominantly low-momentum Ops ($F > 0.5$) with respect to high-momentum ones ($F \leq 0.5$) is shown in figure 6(b). There is also in this case a tendency to spanwise organization, although the convergence of the PDF is poor because only 41% of the low-momentum Ops have a high-momentum neighbor satisfying (8).

The relative position between Ops and Qs is shown in figure 6(c). Most Ops (98%) have at least a Q satisfying (8), and 50% of these Qs are closer than the mean diameter of the reference Op . Essentially Ops and Qs are collocated.

Finally, the distance from Ops to the closest sweep-ejection pair, defined as in [2], is examined in figure 6(d). In this case, the center of the pair is defined as

$$\mathbf{x}_c^{(p)} = \frac{\mathbf{x}_c^{(Q_2)} + \mathbf{x}_c^{(Q_4)}}{2}, \quad (9)$$

and its size is defined as the mean of the wall-normal size of the two components of the pair. Most (87%) Ops have a closest Q -pair satisfying (8) and figure 6(d) shows that most Q -pairs are found within the mean length and width of

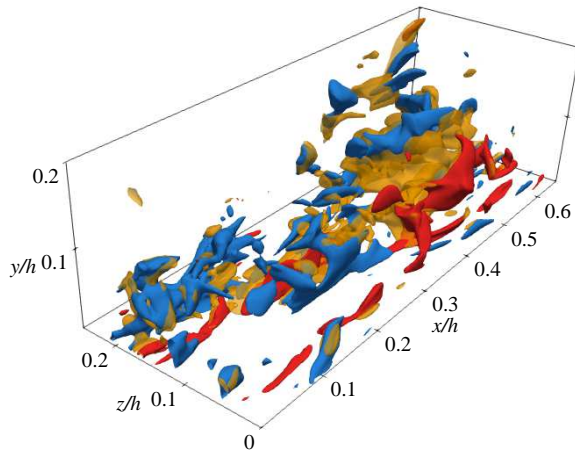


FIG. 7. Instantaneous three-dimensional representation of a strong Op (yellow central object), and its closest sweep (red) and ejection (blue). Flow is from lower-left to upper-right. $Re_\tau = 2003$.

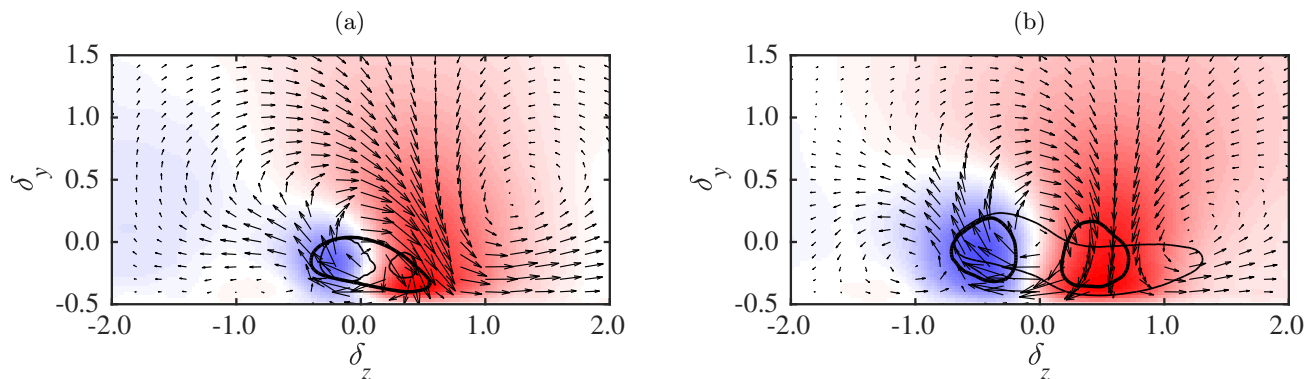


FIG. 8. (a) Cross section at $\delta_x = 0$ of the conditionally averaged field around tall attached Ops in the logarithmic region, looking in the direction of the flow. The color background is \tilde{u} , increasing from blue to red; arrows are the velocity in the cross-plane; the heavier contour is $\tilde{\phi}_{xy}^+ = -2.1$, and the lighter double one is $\tilde{uv}^+ = -2.1$. (b) As in (a), for the conditionally averaged field around tall attached sweep-ejection pairs in the logarithmic region. Symbols are as in (a), but the heavier double contour is $\tilde{uv}^+ = -1.3$, and the lighter one is $\tilde{\phi}_{xy}^+ = -1.3$. $Re_\tau = 934$.

the reference Op . As with individual Qs , Ops and Q -pairs overlap.

This result is consistent with section III, which showed that attached Ops are twice wider than Qs , but not taller, and with section IV, where we found that most Ops intersect both high- and low-momentum regions. Together with the results in figure 6, the logical conclusion is that tall attached Ops correspond to the sweep-ejection pairs discussed in [2]. A representative example of this instantaneous configuration is shown in figure 7, where an Op is seen spanning the sweep and the ejection in a pair. This arrangement will be confirmed by the conditional fields in the next section.

VI. CONDITIONALLY AVERAGED FIELDS

We next consider the conditionally averaged flow field around Ops . As was the case with the comparable conditional fields around Q -pairs in [2, 17], this implies defining both a common center and a common scale for the individual objects, so that the conditional average is a scale-less function of a dimensionless vector coordinate δ . Thus, the

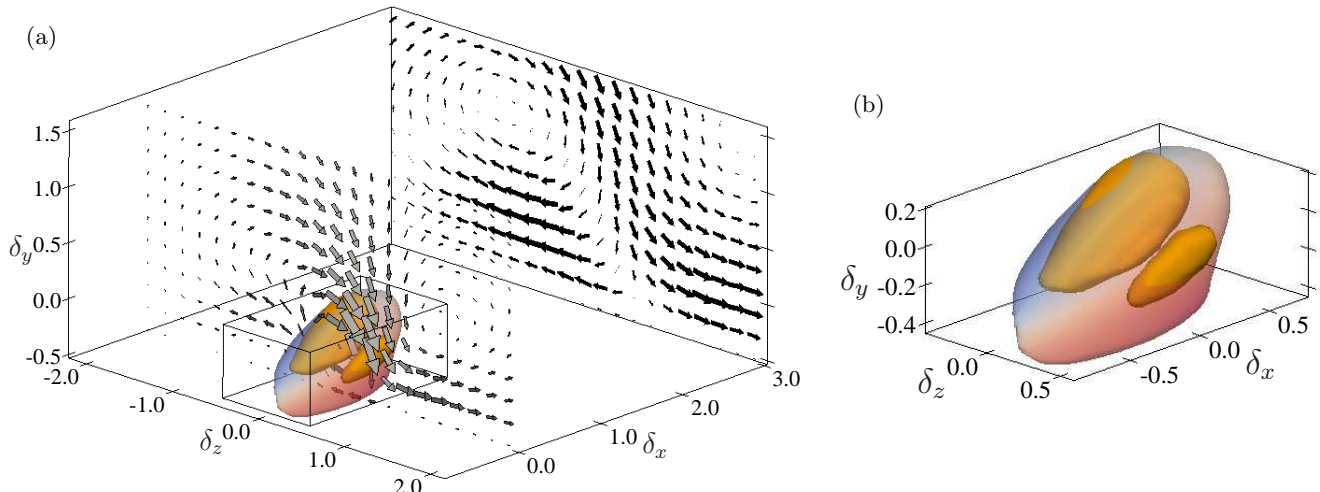


FIG. 9. (a) Three-dimensional plot of the conditionally averaged field around tall attached *Ops* in the logarithmic layer. The translucent isosurface is $\widetilde{\phi}_{xy}^+ = -2.1$, colored by \widetilde{u} ; the yellow solid isosurfaces are $\widetilde{uv}^+ = -2.1$; arrows are the conditional cross-flow velocity: gray ones at $\delta_x = 0$, and black ones at $\delta_x = 3$. Flow is from lower-left to upper-right. (b) Enlargement of the smaller sub-box in (a). $Re_\tau = 934$.

conditional field for a set of N individual fields $q^{(i)}(\mathbf{x})$, is

$$\widetilde{q}(\boldsymbol{\delta}) = N^{-1} \sum_{i=1}^N q^{(i)}(\Delta_y^{(i)} \boldsymbol{\delta} + \mathbf{x}_c^{(i)}), \quad (10)$$

where $\mathbf{x}_c^{(i)}$ is the center of the box circumscribing the i -th object, so that

$$\boldsymbol{\delta} = (\mathbf{x} - \mathbf{x}_c^{(i)}) / \Delta_y^{(i)}. \quad (11)$$

Individual fields are centered, rescaled with the height of its object, $\Delta_y^{(i)}$, and averaged. In computing the conditional fields around Q -pairs in [2, 17] it was found convenient to take advantage of the statistical spanwise symmetry of the flow to reorient each pair so that the sweep is always on the same orientation with respect to the flow direction. We have seen that sweeps and ejections are not relevant for *Ops*, but individual *Ops* can be reoriented so that the highest u is always on the right-hand side, looking in the direction of the flow. To avoid the indeterminacy of this reorientation for *Ops* with $F \approx 0$ or $F \approx 1$, which we saw in figure 5 to be high in number but low in volume, only objects with $0.2 < F < 0.8$ are considered for the conditional fields.

Figure 8(a) shows a section through the $\delta_x = 0$ cross-flow plane of the conditional field around tall attached *Ops* in the logarithmic layer. The colors indicate \widetilde{u} and the arrows are the cross-flow velocity. The average position of the *Op* is given by the heavy contour of $\widetilde{\phi}_{xy}$, which intersects both the high- and the low- u region. It has a single peak near the center of the conditional box, whose position is approximately independent of the choice of the δ_x slice and of the contour magnitude. The position of the associated Qs is marked by the lighter contours of \widetilde{uv} , which has two peaks corresponding to the average location of the sweep and of the ejection. The cross-flow velocities form a circular roller around the box center, reminiscent of the conditional rollers associated with sweep-ejection pairs in [2, 17].

For completeness, figure 8(b) shows the conditionally averaged velocity field around a sweep-ejection pair, confirming the similarity of the flow around *Ops* and Q -pairs. It includes the mean position of the associated *Op*, in the form of a line contour of $\widetilde{\phi}_{xy}$, and it is clear from figure 8(a,b) that *Ops* and sweep-ejection pairs are collocated on average.

Figure 9 shows the three-dimensional counterpart to the conditional field in figure 8(a). There is a strong sweep-ejection pair at the same location as the conditional *Op*. As seen from the arrows at the two cross planes, the circular motion in fig. 8(a) is part of an inclined quasi-streamwise roller, whose orientation can be evaluated by tracking the maximum of the averaged fluctuation vorticity¹, $|\widetilde{\omega}|$. A least-square fit to these local maxima in $0 \leq |\delta_x| \leq 1$ results in

¹ Note that $\widetilde{\omega}$ is different from the vorticity of the conditional velocity $\nabla \times \widetilde{u}$, because of the variable rescaling of the spatial coordinates

a roller inclined at 24° to the wall, and tilted 7.9° towards the low-momentum side. These angles are approximately twice larger than those of other streamwise eddies described in the literature [20, 21], but comparable, for example, to the inclination of the roller of large detached pairs in [17]. That the different results do not agree in detail is not particularly surprising. They are defined by different procedures, including, for example, the present restriction to the logarithmic layer, and it was noted in [21] that the inclination of eddies depends on how they are defined and on the length scales being considered.

VII. CONCLUSIONS

We have presented in this paper a detailed comparison between the intense structures (*Ops*) of the alternative momentum flux ϕ_{xy} defined in [7], and the classical quadrant structures (*Qs*) based on the tangential Reynolds stress uv . Since both fluxes are equivalent in the mean, the emphasis has been on identifying similarities and differences between their intense structures, with a view to ascertaining which of their properties are associated with a particular flux definition, and which ones are more general, presumably characteristic of the momentum flux as such.

Even if the one- and two-point statistics of the two quantities are known to differ considerably [7], the two types of structures share many characteristics. For example, objects large enough to attach to the wall are responsible for most of the momentum transfer in both cases, and those mostly located within the logarithmic layer form self-similar families characterized by fixed aspect ratios, rather than by a fixed size. These results are found to be independent of the Reynolds number for the two cases considered in this work.

However, the tall attached *Ops* are twice wider than the *Qs*, although not taller, and they intersect both high- and low-momentum regions, while *Qs*, because of their definition, tend to be associated with one or with the other. A consequence is that it is difficult to classify *Ops* into the equivalent of the sweeps and ejections found for *Qs*.

In fact, the PDFs of the relative positions of *Ops* with respect to other *Ops*, as well as with respect to *Qs* and to sweep-ejection pairs, strongly support the idea that most *Ops* are manifestations of the same phenomenon as the sweep-ejection pairs. Both are associated with an inclined conditional roller in the border between a high- and a low-speed streak.

We should recall at this point that the purpose of the paper was to test the relevance of the classical quadrant analysis of momentum transfer based on the local Reynolds stress. As we mentioned in the introduction, any gross violation of the hypothesis that the local uv product is representative of the average Reynolds stress would throw doubt, for example, on the validity of the friction velocity as a velocity scale. It is reassuring that none has been found using a different definition of the local flux, but it would be unwise to expect the same to be true for all possible flux definitions. Since fluxes are only determined up to an arbitrary solenoidal tensor, it is clear that we can add a very large spurious component that locally overwhelms the Reynolds stress, and therefore changes all the structures based on the local flux intensity without changing the mean. The question is whether the spurious component in the classical uv product is enough to invalidate the conclusions that have been accumulated in the literature about the dynamical significance of sweeps and ejections. The optimal fluxes, which are designed to minimize the magnitude of the flux and therefore of any added sterile component, should give a fair estimate of the ambiguities involved in both cases.

A related question is why there are such relatively mild differences between the structures of both flux definitions even if the statistics differ considerably. Part of the reason is simply algebraic. It was mentioned in [7] that much of the intermittency of uv has to do with it being a quadratic quantity. This makes its relative maxima stronger than those of ϕ_{xy} , but has much less influence on the lower flux levels used to define the surface of the structures. A more important difference is the amount of momentum backscatter, which was shown in [7] to be considerably lower for ϕ_{xy} than for uv . As mentioned in the previous paragraph, the reason for defining the optimum fluxes is to minimize spurious components, and, from this point of view, backscatter could be considered an artifact of using uv as a local momentum marker. From the PDFs in [7] the difference is mostly in the weaker levels, but it also appears in the relative volumes of the counter- and co-gradient strong structures in Table II, where the volume ratio V^+/V^- is approximately twice larger for *Qs* as for *Ops*.

Our results indicate that the strong co-gradient coherent structures of the momentum flux and the associated streamwise rollers are robust with respect to the definition of the fluxes, and are truly representative of flow features in the logarithmic layer. They also suggest that sweeps and ejections should not be studied as individual objects, but as members of a composite structure containing both.

ACKNOWLEDGMENTS

This work was supported by the Coturb project of the European Research Council (ERC-2014.AdG-669505), and performed in part during the 2017 Coturb Turbulence Summer Workshop at the UPM. A preliminary version of this manuscript appeared in the proceedings of the Workshop. The stay of Mr. Osawa at Madrid was partially funded by the Erasmus Mundus EASED program (Grant 2012-5538/004-001) coordinated by CentraleSupélec.

-
- [1] J. M. Wallace, H. Eckelmann, and R. S. Brodkey, “The wall region in turbulent shear flow,” *J. Fluid Mech.* **54**, 39–48 (1972).
 - [2] A. Lozano-Durán, O. Flores, and J. Jiménez, “The three-dimensional structure of momentum transfer in turbulent channels,” *J. Fluid Mech.* **694**, 100–130 (2012).
 - [3] A. Lozano-Durán and J. Jiménez, “Time-resolved evolution of coherent structures in turbulent channels: characterization of eddies and cascades,” *J. Fluid Mech.* **759**, 432–471 (2014).
 - [4] W. W. Willmarth and S. S. Lu, “Structure of the Reynolds stress near the wall,” *J. Fluid Mech.* **55**, 65–92 (1972).
 - [5] A. Tsinober, “On one property of Lamb vector in isotropic turbulent flow,” *Phys. Fluids A* **2**, 484–486 (1990).
 - [6] C. W. Hamman, J. C. Klewicki, and R. M. Kirby, “On the Lamb vector divergence in Navier–Stokes flows,” *J. Fluid Mech.* **610**, 261–284 (2008).
 - [7] J. Jiménez, “Optimal fluxes and Reynolds stresses,” *J. Fluid Mech.* **809**, 585–600 (2016).
 - [8] J. Bardina, *Improved turbulence models based on large eddy simulation of homogeneous, incompressible, turbulence flows*, Ph.D. thesis, Stanford Univ. (1983).
 - [9] J.-Z. Wu, Y. Zhou, X.-Y. Lu, and M. Fan, “Turbulent force as a diffusive field with vortical forces,” *Phys. Fluids* **11**, 627–635 (1999).
 - [10] J. Jiménez and S. Hoyas, “Turbulent fluctuations above the buffer layer of wall-bounded flows,” *J. Fluid Mech.* **611**, 215–236 (2008).
 - [11] A. A. Townsend, *The structure of turbulent shear flow*, 2nd ed. (Cambridge U. Press, 1976).
 - [12] J. C. del Álamo, J. Jiménez, P. Zandonade, and R. D. Moser, “Scaling of the energy spectra of turbulent channels,” *J. Fluid Mech.* **500**, 135–144 (2004).
 - [13] S. Hoyas and J. Jiménez, “Scaling of the velocity fluctuations in turbulent channels up to $Re_\tau = 2003$,” *Phys. Fluids* **18**, 011702 (2006).
 - [14] F. Moisy and J. Jiménez, “Geometry and clustering of intense structures in isotropic turbulence,” *J. Fluid Mech.* **513**, 111–133 (2004).
 - [15] J. C. del Álamo, J. Jiménez, P. Zandonade, and R. D. Moser, “Self-similar vortex clusters in the logarithmic region,” *J. Fluid Mech.* **561**, 329–358 (2006).
 - [16] J. A. Sillero, *High Reynolds numbers turbulent boundary layers*, Ph.D. thesis, U. Politécnica Madrid (2014).
 - [17] S. Dong, A. Lozano-Durán, A. Sekimoto, and J. Jiménez, “Coherent structures in statistically stationary homogeneous shear turbulence,” *J. Fluid Mech.* **816**, 167–208 (2017).
 - [18] J. Jiménez, “Coherent structures in wall-bounded turbulence,” *J. Fluid Mech.* **842**, P1–P100 (2018).
 - [19] M. Tanahashi, S.-J. Kang, T. Miyamoto, S. Shiokawa, and T. Miyauchi, “Scaling law of fine scale eddies in turbulent channel flow at to $Re_\tau = 800$,” *Int. J. Heat Fluid Flow* **25**, 331–340 (2004).
 - [20] J. Jeong, F. Hussain, W. Schoppa, and J. Kim, “Coherent structures near the wall in a turbulent channel flow,” *J. Fluid Mech.* **332**, 185–214 (1997).
 - [21] J. A. Sillero, J. Jiménez, and R. D. Moser, “Two-point statistics for turbulent boundary layers and channels at Reynolds numbers up to $\delta^+ \approx 2000$,” *Phys. Fluids* **26**, 105109 (2014).